




# The role of climate and population change in global flood exposure and vulnerability

Received: 20 November 2023

Accepted: 24 January 2025

Published online: 03 February 2025

 Check for updates

Justin S. Rogers  , Marco P. Maneta, Stephan R. Sain, Luke E. Madaus & Joshua P. Hacker 

Flooding is a pervasive natural hazard with wide-ranging impacts on society. Using a high-resolution global flood model considering coastal, fluvial, and pluvial hazards, we clarify the role of climate effects versus population growth effects in changing flood exposure. Between 2020 and 2100, the population likely exposed to 1% annual risk (100-year) flood hazard will increase from 1.6 to 1.9 billion people. Of this change from the 2020 exposure, we attribute 21.1% to climate change, 76.8% to population change, and 2.1% to both climate and population change. The largest driver of uncertainty in exposure is population change, while climate change remains a smaller but still important driver. The global increase in exposure between 2020 and 2100 is primarily driven by low-GDP regions, and by 2100 the lowest GDP areas will make up 63% of the exposure both overall and in urban areas. Urban areas are especially vulnerable in nearly all global regions, and urban areas sensitive to extreme events are expected to see a 33% increase in population exposure. This study highlights the vast inequities in flood exposure, and future work should direct resources and strategies toward sustainable risk mitigation in these areas.

Floods are pervasive natural disasters that cause damage to infrastructure, unsafe living conditions, and injury to populations. Losses from storms and floods have steadily increased over the past decades, with losses in 2017 costing the global economy over 140 billion USD<sup>1</sup>, and the subsequent four out of five years (2018 through 2023) having losses of over 100 billion USD annually<sup>2</sup>. While these impacts in our present time are severe, more intense and frequent flood events fueled by climate change and population growth in flood-prone areas are expected to further increase these risks in the coming decades<sup>3,4</sup>. At a global scale, floodplains are being altered at a substantial rate, which is expected to exacerbate flood risk<sup>5</sup>. Additionally, the number of people living in flood-prone and urban regions is growing faster than the number living in other regions<sup>6,7</sup>. Global flood models are critical to understanding these risks both in their severity and location globally.

While flood models contain inherent limitations and approximations, their use as a tool for understanding future flood impact trends is invaluable. Numerous flood models have been developed at both regional<sup>8–11</sup> and global<sup>3,4,12–18</sup> scales to evaluate the impacts of climate

change on flood risk. An inherent challenge is model resolution, whereby finer resolution models have additional computational demands that limit their coverage, while coarser models have broader (often global) coverage at reduced fidelity<sup>11</sup>. A second fundamental challenge is the availability of high-quality digital elevation models (DEMs), which have a large impact on flood model accuracy<sup>19,20</sup>.

Flooding that occurs from coastal, fluvial, and pluvial sources is influenced by climate change. Coastal ocean and lake flooding occurs from the effects of sea level, lake levels, tides, storm surge, and waves, with climate impacts resulting primarily from sea-level rise and changing atmospheric forcing. Tropical cyclone-prone regions are especially at risk<sup>21</sup>. Fluvial flooding arises within river networks as a result of large-scale rainfall-runoff or snowmelt processes<sup>18</sup>, while pluvial flooding results from local watershed rainfall-runoff processes typically associated with high-intensity, short-duration storms<sup>10</sup>. In large-scale flood models, each hazard source is typically evaluated separately and then merged to create a combined exposure prediction. This independent modeling strategy is used because compound flood events are challenging to model over large areas.

Global climate models (GCMs) are often used to inform the boundary forcing for flood models that model exposure based on climate projections. Over the past several decades, global flood models have evolved to have increasingly higher resolution, incorporate updated GCM results, and include multiple flood hazards<sup>3,4,12–18,22</sup>.

Flooding has substantial adverse impacts on society<sup>23</sup>. Global populations are expected to increase from 7.8 billion people in 2020 to an estimated 10.4 billion people in 2100<sup>24</sup>. Current trends from remote-sensing data show that the number of people living in floodplains is growing quickly<sup>6,25</sup>. The global exposure to high flood risk was recently estimated at 1.8 billion people, or approximately one in five people on Earth<sup>26</sup> and exposure to flood risk is particularly concentrated among lower-income households globally<sup>23</sup>. A similar study focusing on the United States found disproportionate annual flood losses of 32 billion USD borne by poorer communities<sup>8</sup>. How communities distribute within flood-prone regions is important to their resilience to extreme events, with increased use of flood defenses creating densely settled areas near flood sources that are sensitive to extreme catastrophic events<sup>27</sup>. In addition, wealthier communities typically have access to resources to construct flood defenses, while poorer communities do not, creating a disparity in protection levels. Because flooding is a highly localized effect, it is critical to conduct impact analyses using a “bottom-up” localized approach rather than a “top-down” macro approach. Here, bottom-up refers to assessing exposure at high-resolution information pertinent at an individual structure level.

With both climate change and growing populations impacting flood risk, characterizing the expected populations at risk of flooding and the relative contributions of climate change vs population change to the overall exposure is critical to inform relevant and effective risk mitigation policy. While meaningful work has been done toward broadly understanding flood risk at a global scale, a gap remains in our collective knowledge of climate change-influenced flooding on populations using combined risk from fluvial, pluvial, and coastal flood sources at a global scale. To address this gap, we present results from modeling flood hazards based on a high-resolution flood model that includes a combined coastal, fluvial, and pluvial framework with global coverage at 90-m resolution and some higher 10-m resolution modeling of pluvial flooding. This work assesses the distribution of exposure in different environments under both climate change and population growth, focusing on urban vs nonurban areas, as well as the vulnerability of global populations to flood risk.

## Results

### Flood inundation changes

Numerical flood inundation and changes to it are based on pixel-level computations. For displaying maps, the data is aggregated to political boundaries typically at Administration Level 2 (Admin2), with some differences depending on country (see Methods). Refer to Fig. 1 for an example of aggregation to Admin2. Population projections are at the national level, while exposure is based on a pixel-level computation and aggregated to Admin2 level when needed.

The combined flood model is validated in the U.S. by comparing with FEMA Base Flood Elevation model results, the coastal flood is compared with coastal ocean and lake observations, and the pluvial flood model is compared with high water mark observations from two historical, rainfall-driven events (see Supplementary Information). Comparison of 100-year water FEMA levels at over 583k riverine and coastal points in the US showed a mean bias of -0.57 m and rmse of 2.08 m. Comparison of 100-year water levels at 798 global coastal ocean and lake locations showed a mean bias of 0.17 m and rmse of 1.26 m. The pluvial flood model was compared to USGS high water marks, where a July 2023 event in the Northeast US had a bias of -0.25 m, and rmse of 1.47 m, and the 2021 Hurricane Ida event showed a bias of 0.70 m and rmse of 1.04 m. Overall, these results show the flood

models compare well to external datasets within a range of bias and error typical for flood models at a global scale<sup>3,4,12–18</sup>.

The inundated area for the three flood hazards (coastal, fluvial, and pluvial) from the 100-year flood hazard and combined flood for both the present data and the expected change in inundated area by the year 2100 for climate scenario SSP2-4.5 (Fig. 2a) is the basis for this analysis. Additional return periods, years, and scenarios are available (see Methods) and would provide different quantitative results, but are omitted for clarity. Tipping points such as ice sheet collapse that may lead to much higher sea levels are also out of this scope.

Considering all sources of flooding, the fraction of the Earth's land surface exposed to a 100-year flood inundation is expected to increase from 11.1% to 11.4% from 2020 to 2100 (Fig. 2a). Coastal ocean and lake flooding shows the greatest relative change in the inundated area, followed by pluvial and fluvial flooding (16.7%, 4.8%, and 1.4%). Pluvial flooding shows the largest uncertainty. While these broad averages suggest somewhat modest increases in inundated areas on average, the effect is concentrated in localized areas that are dramatically different from the global average.

The world's ocean and lake coastlines at low and mid-latitudes will experience increases in coastal inundated areas due to the effects of sea level rise, while high-latitude inundated coastal areas will decrease or remain constant (Figs. 3a, 4a), consistent with sea level rise patterns and vertical land motions<sup>28</sup>. The effects of fluvial flooding cover many areas globally, and the expected change in the inundated areas varies depending on the region (Figs. 3b, 4b). In some large basins with a general drying trend, such as central Asia and central North America, event intensification cannot overcome the hydrologic deficit to generate more flooding. This creates lower future fluvial inundation in some regions. Pluvial flooding affects the majority of land areas globally, with primarily increasing inundated areas (Figs. 3c, 4c). Pluvial flooding can increase from small and intense storms even under drier average conditions. Changes in fluvial and pluvial flooding are driven by expected climatic changes in precipitation and land-use patterns. The net effect of combined coastal ocean and lake, fluvial, and pluvial flooding is broad flood risk over the globe (Fig. 3d), and increasing inundated area in most regions of the world, with some exceptions (Fig. 4d).

### Population exposed

Based on the population exposure at the aggregate political boundaries (Fig. 1d), the number of people exposed (PE) to the 100-year flood (see Methods) is estimated at 1.6 billion in 2020, and expected to increase to 1.9 billion by 2100 (Fig. 2c). Here, we define exposure as the number people at risk of the 100-year flood hazard, considering flood defenses where available in the model (see methods). While the total PE is increasing from 2020 to 2100, with expected increases in the global population from 7.8 to 10.3 billion people (Fig. 2b), the relative percentage of the population exposed to flooding will decrease from 20.5% to 18.4%. This decrease is primarily driven by changes in population, which can vary regionally. Population is expected to decline in eastern Asia and increase in Africa and South Asia (Figs. 3e, 4e). Inundated area is expected to increase in those areas throughout the century due to climate effects (Fig. 4d).

In 2020, the relative uncertainty in the 100-year flood area (Fig. 2a) is greater than the relative uncertainty in population (Fig. 2b); and thus flooding is the largest driver in exposure uncertainty for the present time. In 2100, the relative population uncertainty is very high compared to the relative 100-year flood uncertainty, and thus populations projections are the largest driver of uncertainty in future exposure.

While some differences in total exposed populations to previous studies are clear, overall, the results are similarly ranked by hazard and of the same order of magnitude. We estimate 1.6 billion people exposed to the present-day 100-year combined flood, which is lower than the 1.81 billion reported by Rentschler et al.<sup>26</sup> We estimate that 1.1

billion people are exposed to fluvial flooding, which is lower than the 1.4 billion reported by Devitt et al.<sup>27</sup> We estimate 0.2 billion people exposed to coastal ocean and lake flooding, while Kirezci et al.<sup>4</sup> report 0.15 billion people exposed. These differences are caused by different model inputs, methodologies, and population datasets.

The percentages of the global population exposed to flooding in 2020 from coastal, fluvial, and pluvial sources are 2.5%, 14.1% and 9.0%, respectively (Fig. 2c). Fluvial flood impacts on PE show the highest values in 2050, while coastal flooding and pluvial flooding increase through the century. Within urban areas, PE is estimated to increase from 0.6 to 0.8 billion by 2050 and then remain fairly constant to 2100 (Fig. 2c). In addition, the ratio between the combined flood total PE and urban PE is relatively constant in time, meaning that PE is expected to remain split between urban and nonurban areas globally (Fig. 2c).

Spatially, the highest values of PE in 2020 were primarily concentrated in Asia, western Europe, coastal North America, and coastal Africa (Fig. 5a). The PE change from 2020 to 2100 shows increasing and decreasing trends, depending on the region (Fig. 5b). The dominant areas with increases are in sub-Saharan Africa, the Middle East, South Asia, and coastal North America. The dominant areas of decreasing PE are in Eastern Asia and Western Europe.

### Climate change versus population change

PE changes result from both climate effects (Fig. 4d), which change the inundated areas, and changes to populations that increase or decrease the number of people living in a given area (Fig. 4e). Using a decomposition of changes to inundated area and population, we separate how each factor affects the total change in PE (see Methods). We project that the population exposed to flooding will increase from 1.6 to 1.9 billion people between 2020 and 2100 (Fig. 2c). Of this 19.0% increase, climate change results in approximately 21.1%, population change results in 76.8%, and the combined effect results in 2.1% of the total change (Fig. 6a).

Within each global region, the effects of climate change are highly variable. On average, the changes in PE from climate are positive, indicating increasing exposure for populations within the floodplain (Fig. 6b). Population change leads to the largest PE increases within Africa, Australia/Oceania and North America, and Central Asia while Eastern Asia and Europe have the largest decreases in PE (Fig. 6c). Note the percent from population change term is primarily a function of country boundary due to the population projections at a country level (see Methods). The joint effect of climate and population change on PE is smaller in magnitude than the other terms and is positive in Africa

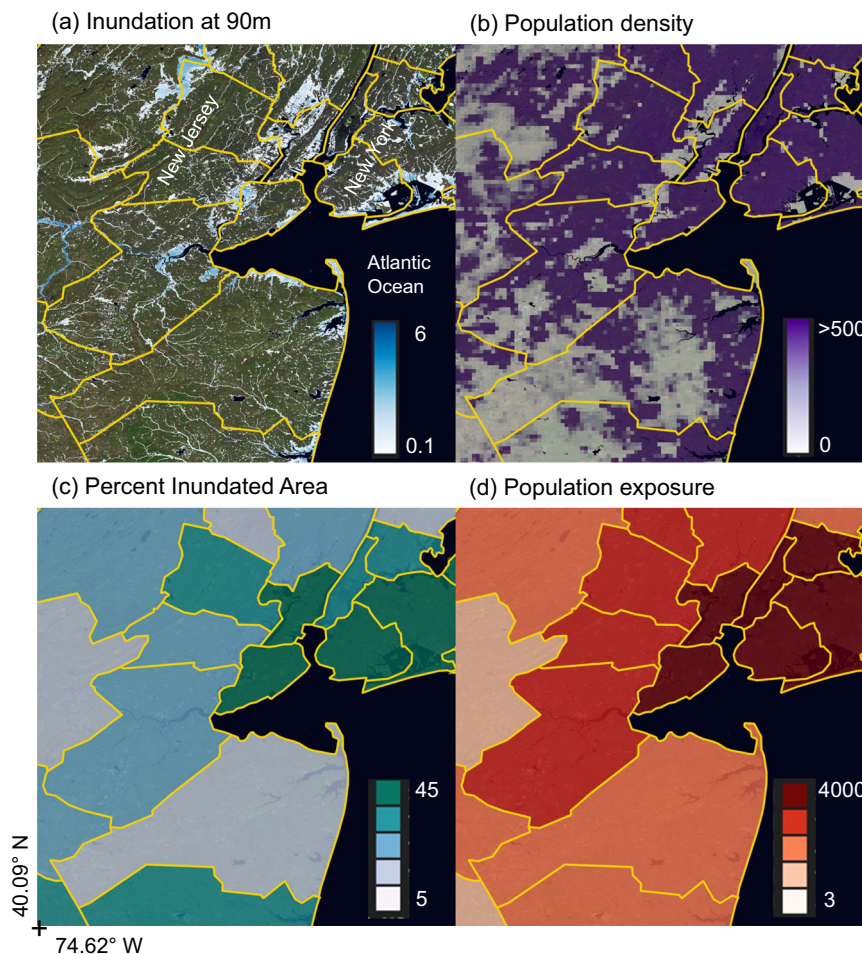


**Fig. 1 | Example inundation and population exposure results in New York City and surrounding area.** **a** 90 m combined flood depth (m) for the 100-year flood hazard, SSP2-4.5 scenario, **b** population density (people/km<sup>2</sup>) where areas greater than 500 indicate an urban environment, **c** aggregate percent inundated area, and **d** aggregate population exposure (people/km<sup>2</sup>) at the political Admin2 (county) level. Note dark blue shading is regions with persistent water (ocean, lakes, rivers) and excluded from flood analysis. Map created using the Free and Open Source QGIS.

Aerial imagery acquired on 30-Nov-2024, from Earth Resources Observation and Science (EROS) Center. (2020). Landsat 8-9 Operational Land Imager/Thermal Infrared Sensor Level-2, Collection 2 [dataset]. U.S. Geological Survey. <https://doi.org/10.5066/P9OGBGM6>. Political boundaries from Runfola et al. (2020) geoBoundaries: A global database of political administrative boundaries. PLoS ONE 15(4): e0231866. (<https://doi.org/10.1371/journal.pone.0231866>) published under CC-BY Attribution 4.0 International license (<https://creativecommons.org/licenses/by/4.0>).

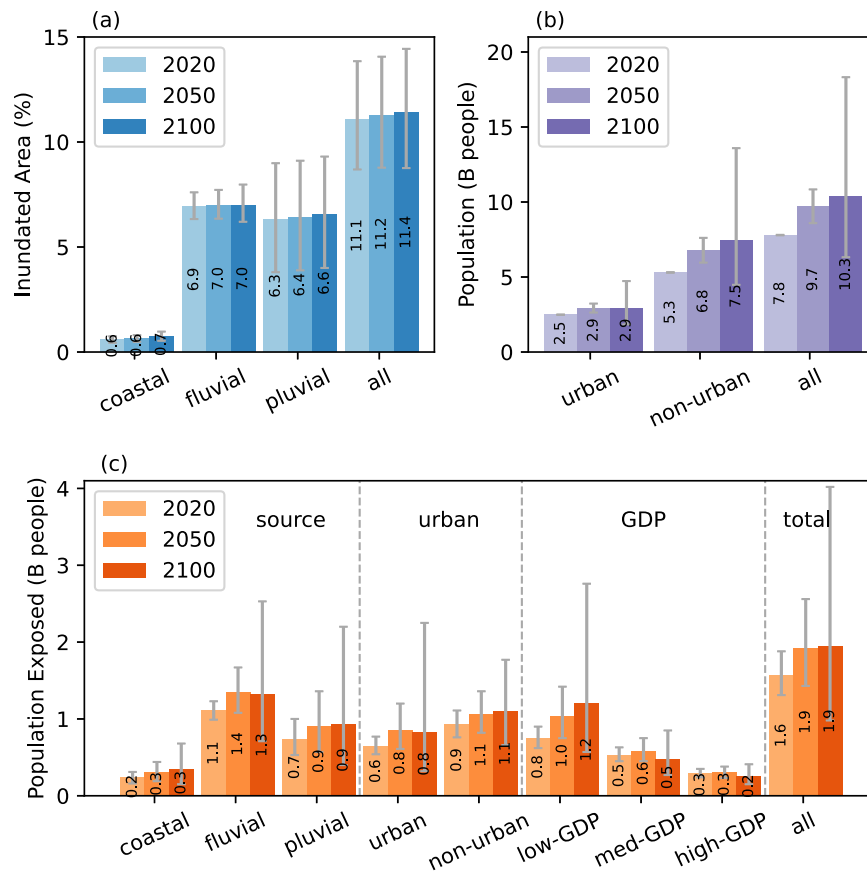


**Fig. 2 | Summary statistics of inundated area, population and population exposed to flooding.** **a** Percent inundated area, **(b)** population (billion people), and **(c)** population exposed to flooding (billion people) from a range of sources, urban and non-urban environment, and across lowest 1/3, medium and highest 1/3

GDP regions for the 100-year flood hazard, SSP2-4.5 scenario. Uncertainty bands represent the 5th/95th percentile flood exposure (i.e. the 5th percentile flood hazard with the 5th percentile population projection). The evaluated Earth land surface ignoring permanent water is 128 M km<sup>2</sup> between +/−72° latitude.

and negative in Eastern Asia, while other regions are highly variable (Fig. 6d).

### Most vulnerable areas

Here, we elucidate which regions are most vulnerable. Rather than computing explicit vulnerability metrics such as damage and loss, for which few to no global datasets exist, we adopt a relative vulnerability approach similar to other studies<sup>29,30</sup> and focus it specifically on PE and GDP (see Methods). We adopt local area GDP within each country as a proxy for the ability of a region to support infrastructure, recover from extreme events, and provide for adaptation and resilience measures<sup>31,32</sup>. The global increase in exposure between 2020 and 2100 is primarily driven by low-GDP regions (Fig. 2c).

Additionally, we conduct an analysis of the sensitivity of inundated areas and population exposure to varying flood event magnitudes (see Methods), which have been shown to correlate with flood sensitivities as well as with societal behavior<sup>27</sup> (Fig. 7a). Low values correspond to areas of population exposure that are frequently exposed to low return period events, while high values correspond to areas not inundated except at the highest return periods and therefore are sensitive to rare events. Geographically, areas that are exposed to flooding relatively frequently (for low return periods) are prevalent. Areas sensitive to extreme events are notably along the US Gulf Coast, Central America, the Amazon River basin, India and Pakistan, Eastern China, Northern Europe, and arid regions of Africa and Australia.

The total expected increase in PE from 2020 to 2100 for all areas is 24% (from 1.6 to 1.9 billion people) (Fig. 7b). In the lowest 1/3 GDP areas, the increase in PE is 50%, and in the 1/3 most sensitive areas to

extreme events, the increase is 25%. Focusing on urban areas, the expected total increase in PE<sub>u</sub> between 2020 and 2100 is 33% (0.6 to 0.8 billion people). In the lowest 1/3 GDP urban areas, the PE<sub>u</sub> increases by 150% (Fig. 7c). By 2100 the lowest GDP areas are expected to make up 63% of the exposure, both overall and in urban areas (Fig. 7b,c).

## Discussion

The results presented here are based on the extent of flood inundation and population exposure from coastal ocean and lake, fluvial, and pluvial sources between 2020 and 2100 at a global scale. Flood model validation results show the flood models compare well to external datasets within a range of bias and error typical for flood models at a global scale. Because of differences in methodology and data, total exposed population estimated here differs somewhat from previous studies, as would be expected. Overall, the results are similarly ranked by hazard and of the same order of magnitude. By presenting the flood exposure from components of flood risk (coastal, fluvial, pluvial) as well as combined flood, we avoid potential double counting of exposure when only one flood risk type is considered, or multiple studies are aggregated.

The distribution of climate impacts on flooding varies by region and flood type. Generally, coastal areas and pluvial-dominated areas will see increased flood risk, while fluvial-dominated areas are strongly dependent on local climatology, a result consistent with other studies<sup>3,4,12–18</sup>. Regionally, the areas with the largest increase in population exposure to floods are in sub-Saharan Africa, the US Atlantic Coast, southern Asia, the Middle East, and southeast Asia. For this study, we selected the SSP2-4.5 (middle of the road) scenario, where

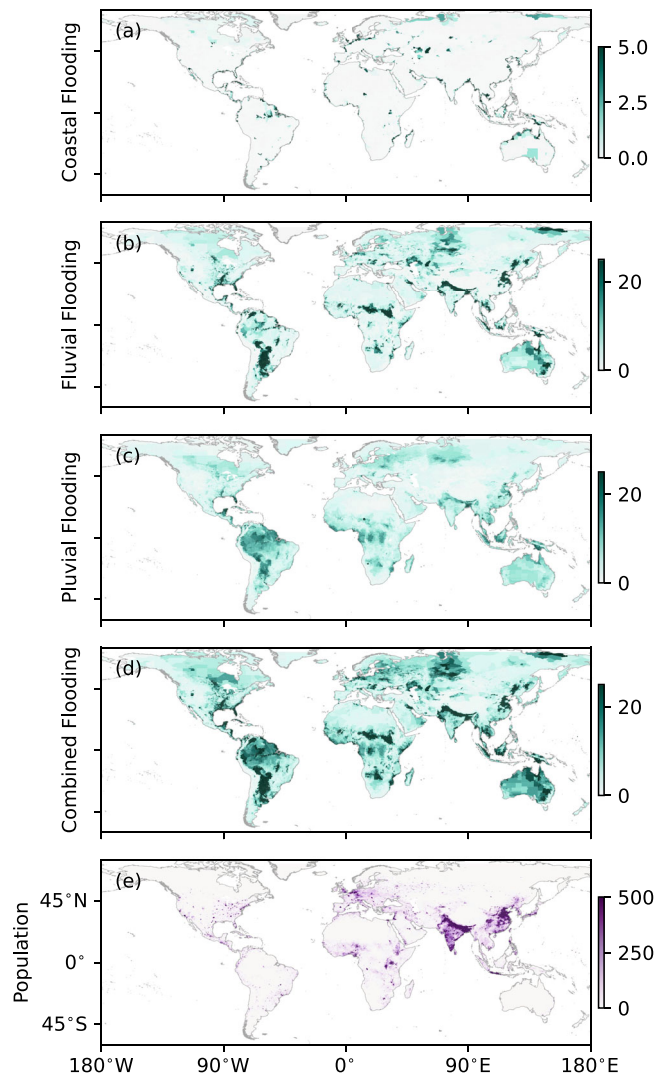


**Fig. 3 | Present-day flood inundation and population globally, shown at political boundary aggregate.** Percent inundated area 100-year flood for (a) coastal ocean and lake flood, (b) fluvial flood, (c) pluvial flood, and (d) combined flood. e Population density (people / km<sup>2</sup>). Note that the color scale in (a) is different from (b–d). Political boundaries from Runfola, D. et al. (2020) geoBoundaries: A global database of political administrative boundaries. PLoS ONE 15(4): e0231866. (<https://doi.org/10.1371/journal.pone.0231866>) published under CC-BY Attribution 4.0 International license (<https://creativecommons.org/licenses/by/4.0>). Figure made with GeoPandas package, Kelsey Jordahl, Joris Van den Bossche, Martin Fleischmann, Jacob Wasserman, James McBride, Jeffrey Gerard, ... François Leblanc. (2020, July 15). geopandas/geopandas: v0.8.1 (Version v0.8.1). Zenodo. <https://doi.org/10.5281/zenodo.3946761>.

global emissions decline by the end of the century. Other climate scenarios will yield different flood impacts, and therefore, this study should not be considered an upper bound on potential impacts in a worst-case climate scenario.

The focus of this work is on the attribution of climate effects versus population growth effects. We find that by the year 2100, 0.3 billion more people will be exposed to the 100-year flood hazard, a result similar to that from other studies<sup>4,26,27</sup>. Of this increase in population exposure given the baseline flood hazard and population, approximately 21.1% is due to climate change, 76.8% is due to population change and 2.1% is due to both climate and population changing simultaneously in a given area. This change in exposure is based on the relative increase from the baseline 2020 exposure. For the present day, flood uncertainty dominates the uncertainty in exposure, as the

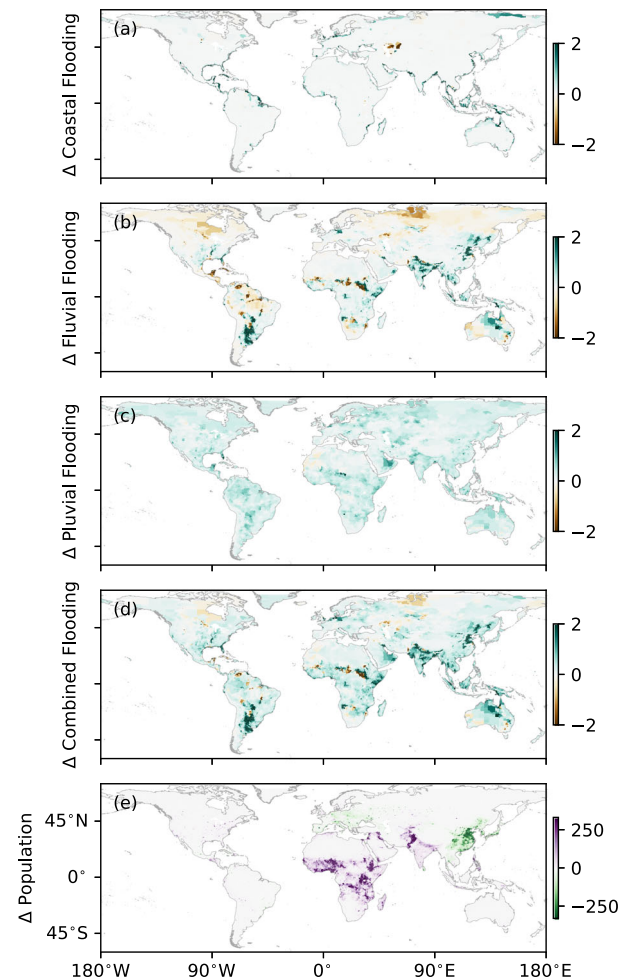


**Fig. 4 | Change in flood inundation and population globally between 2020 and 2100 for climate scenario SSP2-4.5, shown at political boundary aggregate.** Change in percent inundated area 100-year flood for (a) coastal ocean and lake flood, (b) fluvial flood, (c) pluvial flood, and (d) combined flood. (e) change in population density (people / km<sup>2</sup>). Political boundaries from Runfola, D. et al. (2020) geoBoundaries: A global database of political administrative boundaries. PLoS ONE 15(4): e0231866. (<https://doi.org/10.1371/journal.pone.0231866>) published under CC-BY Attribution 4.0 International license (<https://creativecommons.org/licenses/by/4.0>). Figure made with GeoPandas package, Kelsey Jordahl, Joris Van den Bossche, Martin Fleischmann, Jacob Wasserman, James McBride, Jeffrey Gerard, ... François Leblanc. (2020, July 15). geopandas/geopandas: v0.8.1 (Version v0.8.1). Zenodo. <https://doi.org/10.5281/zenodo.3946761>.

population data is well-constrained. In future years, the uncertainty in population exposure is dominated by population projections, which are highly uncertain compared to the flood projections. Thus, globally the largest driver of uncertainty in exposure is population change, while climate change remains a smaller but still important driver.

At a continental level, population change is highly variable depending on region and other factors. Africa is expected to see the greatest increases in total population by 2100 and thus large increases in population exposure. Climate change increases population exposure in nearly all areas. Focusing specifically on different environmental regions, we find that most changes in population exposure will occur in coastal-fluvial transition regions (i.e., cities adjacent to estuaries or along rivers near the ocean). In upland regions, we find similar risk distributed along pluvial and fluvial sources (see Supplementary Information).

The population changes used in this study assume the same spatial distribution of population density and the same growth rate

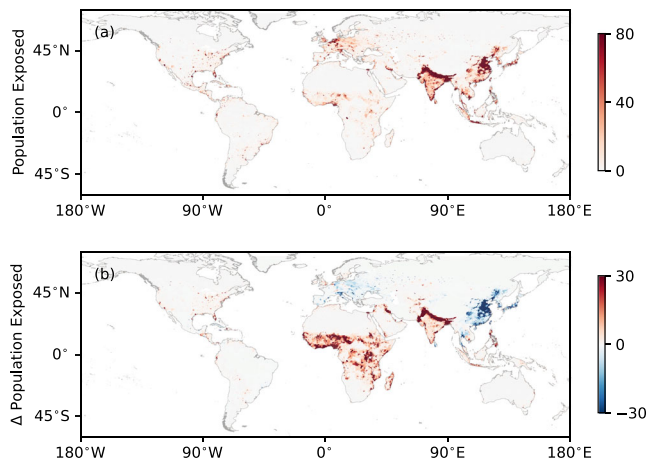


**Fig. 5 | Population exposed to flooding for the present day and future change in population exposure.** Population exposed to flooding (people/km<sup>2</sup>) in (a) the present day and (b) the change in population exposed to flooding between 2020 and 2100. All results for the 100-year flood climate scenario SSP2-4.5. Political boundaries from Runfola et al. (2020) *geoBoundaries: A global database of political administrative boundaries*. PLoS ONE 15(4): e0231866. (<https://doi.org/10.1371/journal.pone.0231866>) published under CC-BY Attribution 4.0 International license (<https://creativecommons.org/licenses/by/4.0>). Figure made with GeoPandas package, Kelsey Jordahl, Joris Van den Bossche, Martin Fleischmann, Jacob Wasserman, James McBride, Jeffrey Gerard, ... François Leblanc. (2020, July 15). *geopandas/geopandas: v0.8.1* (Version v0.8.1). Zenodo. <https://doi.org/10.5281/zenodo.3946761>.

within each country. Thus, future adaptation to climate, changes to locations of urban centers, and rural-to-urban migration in the coming decades are not considered, and the urban population exposure estimates in this study are likely underestimates. Additionally, we do not consider future changes to local land use, such as urbanization, apart from large-scale adaptations within the GCMs. Thus, future estimates of flooding for pluvial and fluvial flooding are likely a lower bound, as areas of higher population density would likely generate higher runoff.

We exclude the effects of storm drains or other stormwater control features in the flood models, which may overpredict flood extents in some urban areas. We include flood defenses for countries where this information is available but assume undefended conditions for areas with no defense information (see Methods). This assumption implies potentially overpredicted flood inundation from coastal and fluvial sources in regions where flood defenses exist on the ground but not in the model. Additionally, a single population scenario (UN medium) and climate scenario (SSP2-4.5) are assumed in this work to illuminate the broad trends, but further study could explore the range of variation among projection scenarios.

The vulnerability of different regions highlights the inequities present in population exposure to current and future flood risks, a similar theme noted for the US in prior work<sup>8,30</sup>. The increase in exposure by 2100 is primarily driven by low-GDP regions. These low-GDP regions also face a disproportionately high population exposure compared to mid- and high-GDP regions. By 2100 the lowest GDP areas will make up 63% of the exposure both overall and in urban areas.

Additionally, we evaluate the relative sensitivity to extreme flood events. Areas that are not often inundated except at the highest return periods are sensitive to extreme events, while areas subject to frequent flood events are more flood-aware<sup>27</sup>. We find increased sensitivity to extreme events in particular regions globally, most notably several large river basins and arid regions. In terms of increased population exposure, urban areas are especially vulnerable to extreme events in nearly all regions. Areas sensitive to extreme events represent 44% of the total population exposure and are expected to see increased population exposure by 33% in urban areas by 2100.

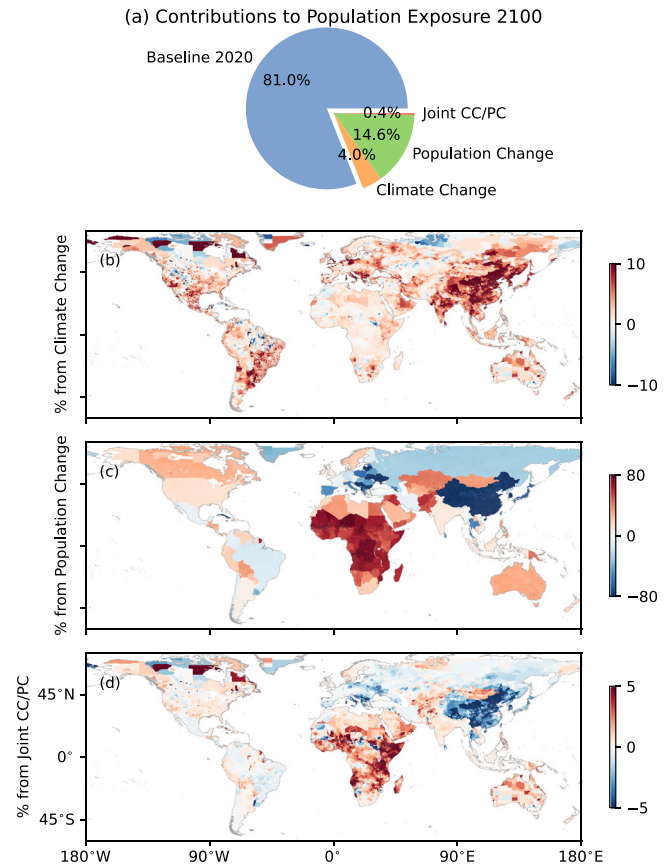


**Fig. 6 | Effects of climate change vs population change on population exposure between 2020 and 2100.** a The contribution of each component to the global average, and the spatial contribution of (b) climate change, (c) population change, and (d) joint effect of climate and population change. Percentages are shown as the contribution of each factor divided by the future 2100 population exposure, positive values are increasing exposure, negative values are decreasing exposure. All results are for the 100-year flood hazard, SSP2-4.5 climate scenario.

The results of this study are a comprehensive assessment of future global population exposure to floods. They highlight the importance of characterizing both the present-day and future climate-influenced flood risks to populations. Low-GDP regions and urban areas are especially vulnerable to flooding from extreme events from both current exposure levels and expected increases in populations at risk. Effective land use strategies should be implemented to ensure that growing populations are building and developing in regions that are protected from future flood risk and implementing resilient strategies to mitigate this risk. In addition, this study highlights the vast inequities in risk exposure, with the relatively lower-income regions being especially vulnerable. For future work, there is a need to account for dynamics in socio-economic development in flood risk assessments, including exposure as well as vulnerability, and additionally exploring potential feedback due to adaptation responses and migration decisions<sup>30</sup>. This should direct resources and strategies toward sustainable risk mitigation in these areas.

## Methods

### Flood modeling

We have developed a global flood model of flood depth inundation throughout the century for coastal ocean and lake, fluvial, and pluvial flood hazards for various years (baseline, 2020 to 2100 at 5-year increments), return periods (10 to 500 years), uncertainty levels (5th, mean, 95th), and climate scenarios (baseline, SSP1-2.6, SSP2-4.5,

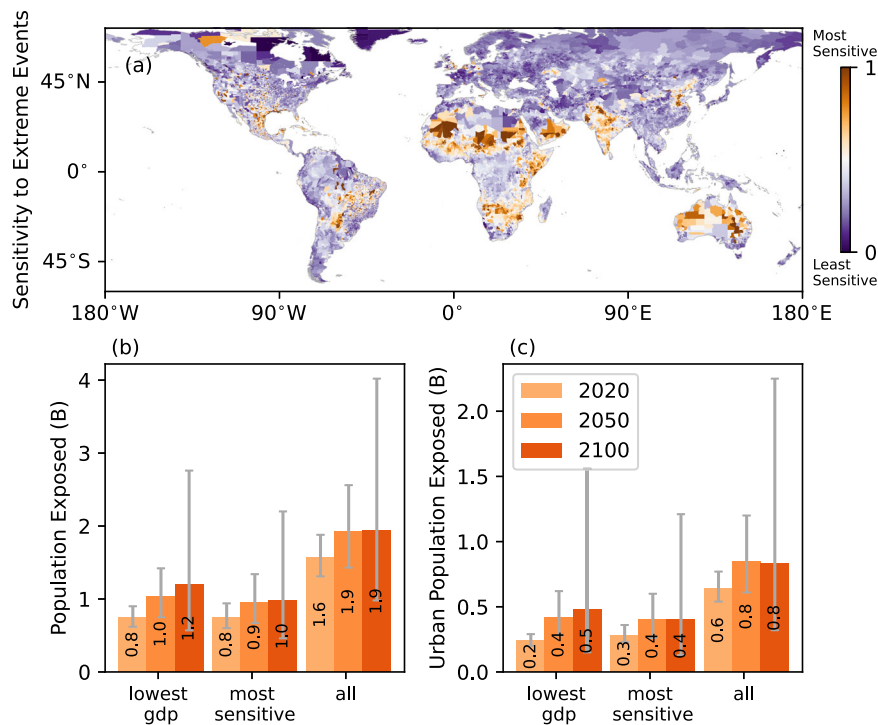


**Fig. 7 | Vulnerability and flood sensitivity to extreme events.** **a** 2020 flood sensitivity to extreme events, **b** population exposed summary, and **c** urban population exposed summary for the 100-year flood hazard, SSP2-4.5 scenario. Uncertainty bands represent the 5th/95th percentile flood exposure (i.e. the 5th percentile flood hazard with the 5th percentile population projection). The lowest GDP is regions with the lowest 1/3 GDP per capita, and the most sensitive is regions with 1/3 highest extreme event sensitivity factor. Political boundaries from Runfola, D. et al. (2020) *geoBoundaries: A global database of political-administrative*

boundaries. *PLoS ONE* 15(4): e0231866. (<https://doi.org/10.1371/journal.pone.0231866>) published under CC-BY Attribution 4.0 International license (<https://creativecommons.org/licenses/by/4.0>). Figure made with GeoPandas package, Kelsey Jordahl, Joris Van den Bossche, Martin Fleischmann, Jacob Wasserman, James McBride, Jeffrey Gerard, ... François Leblanc. (2020, July 15). *geopandas/geopandas: v0.8.1 (Version v0.8.1)*. Zenodo. <https://doi.org/10.5281/zenodo.3946761>.

SSP5-8.5). The digital elevation model (DEM) used to define the Earth's surface was based on a wide variety of publicly available sources, including MERIT<sup>19</sup>, Coastal90 dem<sup>20</sup>, USGS NED<sup>33</sup>, and other publicly available datasets in Europe, Canada, Japan, and Australia. The model has global coverage and is based on a 90-m grid scale using the EGM96 geoid. Some areas have enhanced modeling at 10-m resolution. We employed separate models for coastal, fluvial, and pluvial flooding, and then combined the results.

### Coastal ocean and lake model

The coastal ocean and lake flood model used multiple climate projection datasets to estimate the effects of sea-level rise and storm surge, tides, and waves on coastal inundation, as well as storm surge and lake levels on lake shoreline inundation. The basis of the model is at coastal points globally (see Supplementary Information Fig. S18), whereby a series of sequential operations were conducted to compute the return-period-based water levels for a range of years and climate scenarios. Data inputs for the coastal ocean and lakes are from separate sources at the coastal points.

### Coastal Ocean

Beginning with a storm surge model (GTSR)<sup>21</sup> which includes tidal effects, the extreme values statistical parameters were debiased using ocean observations (GESLA-3)<sup>34</sup> at 14,799 coastal ocean points globally. Next, we included the effects of parameterized wave setup<sup>22</sup> using validated data from the WaveWatch III Hindcast<sup>35</sup>. We then included relative sea level rise projections from the IPCC AR6 projections<sup>28</sup> using nearest neighbor interpolation (which includes estimates of local land movement, glacial isostatic adjustment, thermal expansion, water storage, etc.).

### Coastal lakes

Lake data was obtained from long-term remote sensing (G-REALM)<sup>36</sup>, and in-situ observations (NOAA, CO-OPS water level observation data) for 656 lakes globally. The short-term variability in historical lake levels was used to define extreme value statistical parameters. While different processes dominate in different coastal lake settings, our general approach is data-driven, extreme value analysis. The long-term lake levels follow the recent trends since 1950 in the near term but are gradually reduced to zero trends towards the end of the century. This is to account for uncertainty in forecast trends using historical data projections, which can arise from the climate but also human water use. Thus, long-term lake levels were based on historical trends without climate scenarios, which is an avenue for future development.

### Combined coastal ocean and lake model

The statistical parameters used to define short-term extreme values, and the long-term water level trends for coastal oceans and lakes were then combined using a joint uncertainty analysis and a Monte Carlo sampling approach.

Wind projections were based on extreme value analysis of downscaled daily maximum wind speed from multiple CMIP6 GCMs<sup>37,38</sup>, specifically with the following models (number of ensemble members indicated in parentheses): ACCESS-ESMI-5 (3), CESM-LENS (40), CESM Med. Ens. (15), CNRM-CM6-1 (6), MIROC6 (50), MPI-ESMI-2 (10), and UKESMI-0 (6). In tropical cyclone (TC)-prone regions, wind projections were supplemented using a very large sample of synthetic TC tracks<sup>39,40</sup> with a parametric TC intensity model adjusted for future climate conditions<sup>41-43</sup>. Parameterized climate effects of changing winds on short-term extreme water level values were applied to both coastal ocean and lake points. We assume wind energy is the primary

driver of short-term water level fluctuations arising from a variety of mechanisms including wind-driven storm surge, wave setup, seiches, etc. This assumption may under- or over-estimate changes in extreme values locally, however, due to weak climate trends for future wind conditions, the impact on the global 100-year coastal water levels is small with no long-term trend and less than 10% variation. In tropical cyclone-prone areas there is a 4% average increase by 2100 and less than 20% variation (see Supplementary Information Fig. SI9).

Finally, datums were adjusted from mean sea level to EGM96 framework using the Mean Dynamic Topography<sup>44</sup>. These coastal water levels were then passed to the inundation model to compute depths of flooding on the grid (see below).

### Fluvial Model

The fluvial flood model is a cascading sequence of hydrologic and hydraulic simulators that derive depths within a river network by routing daily runoff from a suite of 27 simulations of the CMIP6 suite of GCMs<sup>37,38</sup> downscaled to one km<sup>2</sup> resolution. The depths within the river network were then passed to the HAND inundation model to compute the depths of flooding on the grid (see below).

Specifically, we used the following models (number of ensemble members indicated in parentheses): ACCESS-ESM1-5 (6), BCC-CSM2-MR (1), CESM2 (1), CMCC-ESM2 (1), EC-Earth3 (1), HadGEM3-GC31-LL (1), INM-CM5-0 (1), IPSL-CM6A-LR (2), KACE-1-0-g (1), MIROC6 (3), MPI-ESM1-2-HR (1), MRI-ESM2-0 (5), NorESM2-MM (1), and UKESM1-0-LL (5). Daily runoff is defined as the excess precipitation and snowmelt available for surface and subsurface runoff after interception, infiltration, ponding, and evapotranspiration losses are subtracted. Daily precipitation runoff was spatially averaged over hydrologic response units based on sub-catchments defined by a vectorized global river network dataset extracted from high-resolution 90-m datasets. The time series of spatially averaged runoff was converted into a time series of lateral flows into the river network using a convolution with a triangular unit hydrograph adapted to local watershed characteristics. Daily time series of lateral inflows were routed through the river network using the Muskingum routing method to obtain daily stream flows. Finally, the fluvial process employed a 1D river channel model to solve for the depth, using a hydraulic model based on a quasi-steady state form of the St. Venant equations, local river geometry cross-sections at 90 m spacing, Manning's roughness, and stream flows. The quasi-steady state form drops the local acceleration from the inertial terms but keeps the convective acceleration term. Backwater effects from boundary conditions at the ocean were considered at high tide. A maximum annual series of stream flows was used to inform the extreme value analysis to determine return periods and associated uncertainty. Channel flow depths associated with maximum stream flow at the desired return periods were used in the inundation algorithm to fill the floodplain.

### Floodplain inundation for fluvial and coastal

The floodplain inundation model used for both fluvial and coastal floods was based on the Height Above Nearest Drainage (HAND) algorithm<sup>45</sup>, which applies flood levels of constant elevation along flow paths. For fluvial floods, we applied the HAND algorithm to simulate propagation away from river channels. The classic application of HAND does not conserve mass because it is typically applied using water elevations obtained from calibrated rating curves at the channel that does not adequately capture the geometry of the floodplain and its effect on energy losses. This can cause unrealistic flood extents. To resolve this limitation, we used the valley-averaged channel and floodplain cross-section to calculate the flow cross-sectional area in the 1D river channel equation. The resulting flow depth (for a given channel slope and roughness) produces an average flow cross-section that when multiplied by the reach length conserves mass (*i.e.* conservation of mass would be perfect if the floodplain cross-section was

constant along the reach length). This causes HAND flood extents to be consistent with mass balance constraints. Discrepancies in the mass balance are introduced when the valley geometry deviates from its average shape at different points along the reach. Thus, the method conserves mass on average at a reach scale, but there is some scatter for individual cross-sections. While it contains limitations, this methodology is a major improvement in the application of the HAND method in rivers.

For coastal ocean and lake floods, HAND simulated flood propagation inland from the coastline, where we added a constant energy dissipation term to reduce storm surge and tides linearly with inland propagation. The energy dissipation term was calibrated based on a wide range of external flood inundation sources of coastal flooding including FEMA and local high-resolution studies.

Thus, the inundation model can be characterized as non-hydrodynamic, mass-conserving at a river reach scale (for fluvial flood), and non-mass-conserving energy-based (for coastal flood). These approximations may lead to differences in inundation at a local scale compared to high-resolution dynamical models, but on average, results compare well to external validation data (see Supplementary Information).

Flood defenses for rivers and coasts were included in the algorithm based on datasets covering the USA, (US National Levee Database, <https://nld.sec.usace.army.mil/>), the Netherlands (<https://www.opendelve.eu/>), portions of the UK (UK Environment AIMS 2020 Spatial Flood Defences for England), France (Bureau de Recherches Géologiques et Minières, Flood Zoning – 2020 Report) and portions of Germany (local government databases Baden-Württemberg, Bremen, Lower Saxony). Flood defense information outside these regions was not available at the time of model development but will be included in future model updates when available. This assumption implies potentially overpredicted flood inundation in regions where flood defenses exist on the ground but not in the model. Additionally, we do not consider future climate adaptation measures or improvements to existing flood defenses in the model. The defense logic was based on a return period protection level under baseline conditions (*i.e.* overtopping occurs if water levels exceed the baseline protection level).

### Pluvial model

The pluvial flood model was forced by global extreme precipitation projections derived from CMIP6 GCM results<sup>37,38</sup>. These extreme precipitation projections were used to simulate the rain-on-grid events.

Specifically, we used the following models (number of ensemble members indicated in parentheses): ACCESS-ESM1-5 (3), CESM2 (3), CESM-LENS (40), CESM Med. Ens. (15), MIROC6 (50), MPI-ESM1-2 (10), and UKESM1-0-LL (6). These were bias-corrected, downscaled to 0.25 degrees, and summarized using a generalized extreme value (GEV) model<sup>46</sup> and associated uncertainty. The pluvial model combined an efficient fill-spill-merge (FSM) algorithm that infills low areas<sup>47</sup> with a modified rational method model used in combination with Manning's equation to approximate overland flow depth<sup>48</sup>. In locations within the USA and Europe where DEM data are available at 10-m resolution, the pluvial model was run at the native higher resolution and then coarse-grained to 90 m. Elsewhere, the model was run at 90 m resolution, which may underestimate pluvial flooding in dense urban areas in the FSM method. We excluded the effects of storm drains or other stormwater control features in the pluvial model. In these cases, the rational method provides a reasonable flooding result for the overland flooding over the pixel on average.

### Combined flood model

The combined flood model result was based on the maximum coastal, fluvial, and pluvial flood depth at each pixel for a given return period, year, and climate scenario. The assumption of maximum depth is based on the probability of occurrence of a flood hazard. Because we

are evaluating flood risk from coastal storm surge events, small-scale high-intensity pluvial flood events, and large-scale medium-intensity fluvial events, these processes are on average independent. Coincident event types are rare, but certainly possible, leading to compound flood hazards. In general, these joint hazards can increase flood levels in areas where hazards overlap. Thus, these results may underestimate flood depth in some selected areas. While modeling compound events is possible computationally at regional scales<sup>11</sup>, it is currently not feasible at global scales, and is a topic of future development.

**Flood model validation**

Extensive validation of the flood results to external datasets is provided in the Supplementary Information.

**Flood exposure**

Based on the flood model depth results, we created a flood mask  $F$  for regions without permanent water,

$$F = (D > \alpha) \cup (W) \tag{1}$$

where  $D$  is the flood depth and  $\alpha$  is a flood threshold considered meaningful for impacts. The lower threshold limit is needed here where pluvial flooding is modeled because nearly all grid cells have some positive depth and are resolved to 1 cm vertical depth resolution. While there is no universal agreement on this threshold, 10 cm is used for this study and is generally assumed to represent a transition from nuisance flooding to flooding potentially causing damage<sup>49</sup>.  $W$  is a mask of typically dry areas based on the seasonal duration of surface water  $S_w$  from the Global Surface Water Explorer dataset at 30 m resolution (<https://global-surface-water.appspot.com/>)<sup>50</sup>,

$$W = S_w < \beta \tag{2}$$

and  $\beta$  is a threshold here selected as 6 months.  $F$  is thus a measure of areas within the modeled floodplain of meaningful depth that are not within permanent water bodies (ocean, lakes, river channels, etc.).

To aggregate the results in a meaningful way, we used the geo-boundaries dataset (<https://www.geoboundaries.org/>) selecting the average administrative level (ADM0,1,2) for each country, which is closest to  $4.2 \times 10^3 \text{ km}^2$  on average on a logarithmic scale. For example, in the USA, this results in the ADM2 level (counties). The inundated area  $I$  over a given area is then given by the sum of the flooded area

$$I_n = \sum F_i dA_i \tag{3}$$

where  $dA$  is the grid cell area.

**Population exposure**

Population used gridded baseline density  $P_d$  at 30 arc-sec resolution (approx. 1 km) (GPWv4, <https://sedac.ciesin.columbia.edu/data/collection/gpw-v4>) for 2020. Future population estimates  $P_T$  (year, country) were based on the United Nations World Population Prospects<sup>24</sup> medium variant projection (<https://population.un.org/wpp/>). For each country and year, we adjusted the summed gridded population to match the UN projection with a correction factor

$$C_p = \frac{P_T}{\sum W_i P_{di}} dA_i \tag{4}$$

The corrected gridded population density  $P$  is then given by

$$P(x, y, yr) = C_p W P_d \tag{5}$$

For statistical analysis, countries are grouped by the United Nations Geographic M49 regions (<https://unstats.un.org/unsd/>), Africa, Asia,

Australia & Oceania, Europe, Latin America & the Caribbean, and North America.

The population exposed ( $PE$ ) to flooding in a given area is then the sum of  $P$  within floodplain  $F$ ,

$$PE = \sum F_i P_i dA_i \tag{6}$$

To distinguish urban vs nonurban areas, we applied a mask  $U$  using a threshold  $\gamma$  of 1500 ppl/km<sup>2</sup> per the World Bank<sup>51</sup>

$$U = P > \gamma \tag{7}$$

Thus, the population exposed to flooding within urban and non-urban areas ( $PE_u, PE_{nu}$ ) is

$$PE_u = \sum F_i P_i U_i dA_i \tag{8}$$

$$PE_{nu} = PE - PE_u \tag{9}$$

If we assume a future condition ( $f$ ) is the result of a base condition ( $b$ ) plus a change,

$$F_f = F_b + dF \tag{10}$$

$$P_f = P_b + dP \tag{11}$$

Substituting these definitions into the expression for some future condition  $PE_f$ ,

$$PE_f = \sum [F_b P_b + F_b dP + dF P_b + dF dP] dA = PE_b + dPE_{pc} + dPE_{cc} + dPE_{joint} \tag{12}$$

where the terms from left to right are population exposed from baseline, population change, climate change, and a joint term from coincident climate and population change. This approach to modify the density assumes that the relative population spatial distribution will remain constant within a country and that society will not spatially adapt to climate change. Population exposure data is generally consistent with results from other studies (see Results).

**Gross domestic product**

The regional gross domestic product was taken from Kummu et al. (2020)<sup>52</sup> gridded GDP per capita ( $G_d$ ) for the year 2015 at 5 arc-min resolution (approx. 9 km). Total country GDP estimates  $G_T(\text{country})$  for 2019 are based on the Penn World Table pwt100 dataset, expenditure-side real GDP at chained PPPs (in 2017 \$M USD)<sup>53</sup>. For each country, we adjust the summed gridded GDP to match the country GDP with a correction factor

$$C_G = \frac{G_T}{\sum G_{di} P_i} dA_i \tag{13}$$

The corrected GDP  $G$  for a given region is then given by

$$G = C_G \sum G_{di} P_i dA_i \tag{14}$$

**Vulnerability**

While there are many definitions of vulnerability, here we define the relative vulnerability of a region as an area having high PE and low G; an area that has a relatively low ability to pay for adaptation or climate infrastructure and high exposure of the population to flooding is particularly vulnerable. Additionally, we conducted an analysis of the

sensitivity of population exposure to varying flood event magnitudes following Devitt et al.<sup>27</sup>, and we fit the population exposure to an exponential form

$$\frac{PE}{PE_{500yr}} = \left[ \frac{\log(\log(r))}{\log(\log(500yr))} \right]^b \quad (15)$$

where  $r$  is the return period of interest, the highest modeled return period (500-year) is used to normalize the function, and  $b$  is the extreme event sensitivity found using the best fit of the 10-, 20-, 100-, and 500-year events for each region. Values of  $b$  less than one are defined as populations exposed to low-frequency flood events, while values greater than one are sensitive to high return period events.

## Data availability

The global flood inundation and population exposure data generated in this study have been deposited in the figshare database under accession code Rogers, Justin; Hacker, Joshua (2024). The role of climate and population change in global flood exposure and vulnerability, <https://doi.org/10.6084/m9.figshare.26980498>.

## References

- Bevere, L., Schwartz, M., Sharan, R. & Zimmerli, P. *Natural Catastrophes and Man-Made Disasters in 2017: A Year of Record-Breaking Losses*. (Swiss Re Institute, 2018).
- Swiss, R. E. Natural catastrophes in 2023: gearing up for today's and tomorrow's weather risks. *Sigma* **1**, (2024).
- Winsemius, H. C. et al. Global drivers of future river flood risk. *Nat. Clim. Chang.* **6**, 381–385 (2016).
- Kirezci, E. et al. Projections of global-scale extreme sea levels and resulting episodic coastal flooding over the 21st Century. *Sci. Rep.* **10**, 11629 (2020).
- Rajib, A. et al. Human alterations of the global floodplains 1992–2019. *Sci. Data* **10**, 499 (2023).
- Jongman, B. The fraction of the global population at risk of floods is growing. *Nature Publishing Group UK* <https://doi.org/10.1038/d41586-021-01974-0> (2021).
- Rentschler, J. et al. Global evidence of rapid urban growth in flood zones since 1985. *Nature* **622**, 87–92 (2023).
- Wing, O. E. J. et al. Inequitable patterns of US flood risk in the Anthropocene. *Nat. Clim. Chang.* **12**, 156–162 (2022).
- Vousdoukas, M. I. et al. Climatic and socioeconomic controls of future coastal flood risk in Europe. *Nat. Clim. Chang.* **8**, 776–780 (2018).
- Rosenzweig, B. R. et al. Pluvial flood risk and opportunities for resilience. *WIREs Water* **5**, e1302 (2018).
- Bates, P. D. et al. Combined modeling of US fluvial, pluvial, and coastal flood hazard under current and future climates. *Water Resour. Res.* **57**, (2021).
- Sampson, C. C. et al. A high-resolution global flood hazard model: A high-resolution global flood hazard model. *Water Resour. Res.* **51**, 7358–7381 (2015).
- Hirabayashi, Y. et al. Global flood risk under climate change. *Nat. Clim. Chang.* **3**, 816–821 (2013).
- Kundzewicz, Z. W. et al. Flood risk and climate change: global and regional perspectives. *Hydrol. Sci. J.* **59**, 1–28 (2014).
- Arnell, N. W. & Gosling, S. N. The impacts of climate change on river flood risk at the global scale. *Clim. Change* **134**, 387–401 (2016).
- Jongman, B., Ward, P. J. & Aerts, J. C. J. H. Global exposure to river and coastal flooding: Long term trends and changes. *Glob. Environ. Change* **22**, 823–835 (2012).
- Alfieri, L. et al. Global projections of river flood risk in a warmer world. *Earths Future* **5**, 171–182 (2017).
- Dottori, F. et al. Development and evaluation of a framework for global flood hazard mapping. *Adv. Water Resour.* **94**, 87–102 (2016).
- Dai Yamazaki et al. A high-accuracy map of global terrain elevations. *Geophys. Res. Lett.* (2017) <https://doi.org/10.1002/2017GL072874>.
- Kulp, S. & Strauss, B. H. Global DEM errors underpredict coastal vulnerability to sea level rise and flooding. *Front. Earth Sci.* **4**, 1–8 (2016).
- Muis, S. et al. A high-resolution global dataset of extreme sea levels, tides, and storm surges, including future projections. *Front. Mar. Sci.* **7**, 1–15 (2020).
- Vitousek, S. et al. Doubling of coastal flooding frequency within decades due to sea-level rise. *Sci. Rep.* **7**, 1399 (2017).
- McDermott, T. K. J. Global exposure to flood risk and poverty. *Nat. Commun.* **13**, 3529 (2022).
- United Nations, Department of Economic and Social Affairs, Population Division. *World Population Prospects 2022*. (2022).
- Tellman, B. et al. Satellite imaging reveals increased proportion of population exposed to floods. *Nature* **596**, 80–86 (2021).
- Rentschler, J., Salhab, M. & Jafino, B. A. Flood exposure and poverty in 188 countries. *Nat. Commun.* **13**, 3527 (2022).
- Devitt, L., Neal, J., Coxon, G., Savage, J. & Wagener, T. Flood hazard potential reveals global floodplain settlement patterns. *Nat. Commun.* **14**, 2801 (2023).
- Intergovernmental Panel on Climate Change (IPCC). Ocean, cryosphere and sea level change. in *Climate Change 2021 – The Physical Science Basis* 1211–1362 (Cambridge University Press, 2023).
- Lewis, Tee et al. Characterizing vulnerabilities to climate change across the United States. *Environ. Int.* **172**, 107772 (2023).
- Reimann, L., Vafeidis, A. T. & Honsel, L. E. Population development as a driver of coastal risk: Current trends and future pathways. *Camb. Prisms Coast. Futures* **1**, 1–23 (2023).
- Montgomery, M. R., Gagnolati, M., Burke, K. A. & Paredes, E. Measuring living standards with proxy variables. *Demography* **37**, 155–174 (2000).
- Noy, I. & Yonson, R. Economic vulnerability and resilience to natural hazards: A survey of concepts and measurements. *Sustainability* **10**, 2850 (2018).
- Gesch, D. B., Evans, G. A., Oimoen, M. J. & Arundel, S. The national elevation dataset. American society for photogrammetry and remote sensing. in 83–110 (USGS Publications Warehouse. <http://pubs.er.usgs.gov/publication/70201572>, 2018).
- Haigh, I. D. et al. GESLA Version 3: A major update to the global higher-frequency sea-level dataset. *Geosci. Data J.* **10**, 293–314 (2023).
- Ortiz-Royero, J. C. & Mercado-Irizarry, A. An intercomparison of SWAN and WAVEWATCH III models with data from NDBC-NOAA buoys at oceanic scales. *Coast. Eng. J.* **50**, 47–73 (2008).
- Birkett, C. M. & Beckley, B. Investigating the performance of the Jason-2/OSTM radar altimeter over lakes and reservoirs. *Mar. Geod.* **33**, 204–238 (2010).
- Eyring, V. et al. Overview of the Coupled Model Intercomparison Project Phase 6 (CMIP6) experimental design and organization. *Geosci. Model Dev.* **9**, 1937–1958 (2016).
- O'Neill, B. C. et al. The Scenario Model Intercomparison Project (ScenarioMIP) for CMIP6. *Geosci. Model Dev. Discuss.* **9**, 1–35 (2016).
- Hall, T. M. & Jewson, S. Statistical modelling of North Atlantic tropical cyclone tracks. *Tellus Ser. A Dyn. Meteorol. Oceanogr.* **59**, 486–498 (2007).
- Bloemendaal, N. et al. Generation of a global synthetic tropical cyclone hazard dataset using STORM. *Sci. Data* **7**, 40 (2020).

41. Chavas, D. R., Lin, N. & Emanuel, K. A model for the complete radial structure of the tropical cyclone wind field. Part I: Comparison with observed structure. *J. Atmos. Sci.* **72**, 3647–3662 (2015).
42. Chavas, D. R. & Lin, N. A model for the complete radial structure of the tropical cyclone wind field. Part II: Wind Field Variability. *J. Atmos. Sci.* **73**, 3093–3113 (2016).
43. Jing, R. & Lin, N. An environment-dependent probabilistic tropical cyclone model. *J. Adv. Model. Earth Syst.* **12**, 1–18 (2020).
44. Jousset, S. et al. New global mean dynamic topography CNES-CLS-22 combining drifters, hydrological profiles and High Frequency radar data. (2023) <https://doi.org/10.22541/essoar.170158328.85804859>.
45. Nobre, A. D. et al. Height Above the Nearest Drainage – a hydrologically relevant new terrain model. *J. Hydrol.* **404**, 13–29 (2011).
46. Coles, S. *An Introduction to Statistical Modeling of Extreme Values*. (Springer, Guildford, England, 2013). <https://doi.org/10.1007/978-1-4471-3675-0>.
47. Barnes, R., Callaghan, K. L. & Wickert, A. D. Computing water flow through complex landscapes – Part 3: Fill–Spill–Merge: flow routing in depression hierarchies. *Earth Surf. Dyn.* **9**, 105–121 (2021).
48. Te Chow, V., Maidment, D. R. & Mays, L. W. *Applied Hydrology*. (ds.amu.edu.et, 1988).
49. Mofstakhari, H. R., AghaKouchak, A., Sanders, B. F., Allaire, M. & Matthew, R. A. What is nuisance flooding? Defining and monitoring an emerging challenge. *Water Resour. Res.* **25**, 881 (2018).
50. Pekel, J.-F., Cottam, A., Gorelick, N. & Belward, A. S. High-resolution mapping of global surface water and its long-term changes. *Nature* **540**, 418–422 (2016).
51. Eurostat and DG for Regional and Urban Policy – ILO, FAO, OECD, UN-Habitat, World Bank. *A Recommendation on the Method to Delineate Cities, Urban and Rural Areas for International Statistical Comparisons*. (2020).
52. Kummu, M., Taka, M. & Guillaume, J. H. A. Gridded global datasets for Gross Domestic Product and Human Development Index over 1990–2015. *Sci. Data* **5**, 1–15 (2018).
53. Feenstra, R. C., Inklaar, R. & Timmer, M. P. The next generation of the Penn World Table. *Am. Econ. Rev.* **105**, 3150–3182 (2015).

## Acknowledgements

We acknowledge the superb technical contributions of the following individuals who made this analysis possible: Fariborz Daneshvar, Ian Davies, Rahul Dhakal, Scott Eilerman, Hannah Hampson, Alexis Hoffman, Tarandeep Kalra, Elizabeth Perry, John Exby, Callie McNicholas, Eleanor Middlemas, Jared Oyler, Joey Pucciarelli, Shannon Reault, Hillary Scannell, Nishanth Shah, Xana Sound, Matthew Woelfle, Galin Yacalis, and Jennifer Yin.

## Author contributions

J.S.R, M.P.M., S.R.S, L.E.M., and J.P.H. conceived the project. J.S.R, M.P.M., S.R.S, and L.E.M. developed the flood model. J.S.R. performed all analyses and wrote the manuscript. J.S.R, M.P.M., S.R.S, L.E.M., and J.P.H. aided in the analysis and editing of the manuscript.

## Competing interests

The authors declare no competing interests. Publishing is not expected to provide revenue or an impact on company valuation. The analysis contained in this manuscript is not a Jupiter product, although some flood hazard data included in Jupiter products is used in the analysis.

## Additional information

**Supplementary information** The online version contains supplementary material available at <https://doi.org/10.1038/s41467-025-56654-8>.

**Correspondence** and requests for materials should be addressed to Justin S. Rogers.

**Peer review information** *Nature Communications* thanks Heejun Chang, Sergiy Vorogushyn and the other, anonymous, reviewer(s) for their contribution to the peer review of this work. A peer review file is available.

**Reprints and permissions information** is available at <http://www.nature.com/reprints>

**Publisher's note** Springer Nature remains neutral with regard to jurisdictional claims in published maps and institutional affiliations.

**Open Access** This article is licensed under a Creative Commons Attribution-NonCommercial-NoDerivatives 4.0 International License, which permits any non-commercial use, sharing, distribution and reproduction in any medium or format, as long as you give appropriate credit to the original author(s) and the source, provide a link to the Creative Commons licence, and indicate if you modified the licensed material. You do not have permission under this licence to share adapted material derived from this article or parts of it. The images or other third party material in this article are included in the article's Creative Commons licence, unless indicated otherwise in a credit line to the material. If material is not included in the article's Creative Commons licence and your intended use is not permitted by statutory regulation or exceeds the permitted use, you will need to obtain permission directly from the copyright holder. To view a copy of this licence, visit <http://creativecommons.org/licenses/by-nc-nd/4.0/>.

© The Author(s) 2025, corrected publication 2025